

The impact of physiological noise on hemodynamic-derived estimates of directed functional connectivity

F. Konrad Schumacher^{1,2,3,4,5}, Carmen Steinborn^{1,2,3,4}, Cornelius Weiller^{1,2,4,5}, Björn O. Schelter^{5,6}, Matthias Reinhard^{4,7}, Christoph P. Kaller^{1,2,4,5,8}

¹ Dept. of Neurology, Medical Center – University of Freiburg, 79106 Freiburg, Germany | ² Freiburg Brain Imaging Center, University of Freiburg, 79106 Freiburg, Germany | ³ Faculty of Biology, University of Freiburg, 79104 Freiburg, Germany | ⁴ Faculty of Medicine, University of Freiburg, 79085 Freiburg, Germany | ⁵ BrainLinks-BrainTools Cluster of Excellence, University of Freiburg, 79110 Freiburg, Germany | ⁶ Institute for Complex Systems and Mathematical Biology, University of Aberdeen, Aberdeen AB24 3UE, UK | ⁷ Department of Neurology, Medical Center Esslingen, Teaching Hospital of the University of Tübingen, Esslingen, Germany | ⁸ Department of Neuroradiology, Medical Center – University of Freiburg, 79106 Freiburg, Germany

Running title: The impact of noise on functional connectivity

Acknowledgement: This work was supported by a grant of the BrainLinks-BrainTools Cluster of Excellence funded by the German Research Foundation (DFG, grant number EXC 1086).

Corresponding author: Dr. Christoph Kaller (christoph.kaller@uniklinik-freiburg.de)

Dept. of Neuroradiology, Medical Center – University of Freiburg, Breisacher Str. 64, 79106 Freiburg, Germany

1 **Abstract**

2 Measuring the strength of directed functional interactions between brain regions is fundamental to
3 understand neural networks. Functional near-infrared spectroscopy (fNIRS) is a suitable method to
4 map directed interactions between brain regions but is based on the neurovascular coupling. It thus
5 relies on vasomotor reactivity and is potentially biased by non-neural physiological noise. To
6 investigate the impact of physiological noise on fNIRS-based estimates of directed functional
7 connectivity within the rostro-caudal hierarchical organization of the prefrontal cortex (PFC), we
8 systematically assessed the effects pathological perturbations of vasomotor reactivity and externally
9 triggered arterial blood pressure (aBP) fluctuations.

10 Fifteen patients with unilateral stenosis of the internal carotid artery (ICA) underwent multi-channel
11 fNIRS during rest and during metronomic breathing, inducing aBP oscillations at .1 Hz. Comparisons
12 between the healthy and pathological hemispheres served as quasi-experimental manipulation of the
13 neurovascular system's capability for vasomotor reactivity. Comparisons between rest and breathing
14 served as experimental manipulation of two different levels of physiological noise that were expected
15 to differ between healthy and pathological hemispheres.

16 In the hemisphere affected by ICA stenosis, the rostro-caudal hierarchical organization of the PFC was
17 compromised reflecting the pathological effect on the vascular and neural level. Breathing-induced
18 aBP oscillations biased the magnitude of directed interactions in the PFC, but could be adjusted using
19 either the aBP time series (intra-individual approach) or the aBP-induced fNIRS signal variance (inter-
20 individual approach). Multi-channel fNIRS hence provides a sound basis for analyses of directed
21 functional connectivity as potential bias due to physiological noise can be effectively controlled for.

22 **Key words**

23 Prefrontal cortex; Hierarchical organization; Directed interactions; Near-infrared spectroscopy;
24 Physiological noise; Stenosis

25 **Abbreviations**

26 arterial blood pressure (aBP); functional magnetic resonance imaging (fMRI); functional near-infrared
27 spectroscopy (fNIRS); prefrontal cortex (PFC); internal carotid artery (ICA); (partial) directed
28 coherence ((P)DC); power spectral density (PSD); vector autoregressive (VAR)

29

30 **Compliance with Ethical Standards**

31 **Conflicts of interest.** The authors declare that they have no conflict of interest.

32 **Funding.** This work was supported by a grant of the BrainLinks-BrainTools Cluster of Excellence
33 funded by the German Research Foundation (DFG, grant number EXC 1086).

34 **Ethical approval.** The study was approved by the local Ethics Committee.

35 **Informed consent.** All patients gave written informed consent prior to participation

36

37 **Introduction**

38 Understanding functional networks of the brain is an ongoing challenge in human neuroscience.
39 Approaches to disentangle the functional dynamics between regions of the human brain are mainly
40 based on non-invasive imaging methods that often face tradeoffs between signal-to-noise ratio,
41 temporal and spatial resolution (Scouten et al. 2006). Given the high spatial but low temporal
42 resolution of the commonly used functional magnetic resonance imaging (fMRI), most extant
43 approaches on connectivity are based on correlative measures. However, a high temporal resolution is
44 particularly critical when the directionalities of functional connections are of interest (Roebroek et al.
45 2005; Mader et al. 2008). Multi-channel functional near-infrared spectroscopy (fNIRS) as an optical
46 method to measure cortical hemodynamics provides such high temporal resolutions, an adequate
47 signal quality and a sufficient spatial resolution to assess large-scale cortical networks.

48 Schumacher et al. (2019) recently demonstrated that Granger-causal cross-spectral analysis (Granger
49 1969; Schelter et al. 2006) of resting-state fNIRS data is a promising approach to characterize the
50 rostro-caudally directed hierarchical organization of the prefrontal cortex (PFC; see also Medvedev,
51 2014). The functional architecture of the PFC is thought to implement different levels of cognitive
52 control by processing information through a rostral-to-caudal hierarchy of neural networks, thereby
53 concretizing abstract ideas into actual actions according to specific rules (Badre and D'Esposito, 2007;
54 Blumenfeld et al., 2013; Christoff and Gabrieli, 2000; Fuster, 2008; Koechlin et al., 2003; for a recent
55 review see Badre and Nee, 2018). Directly assessing the mode of action of the PFC and its integrity
56 with a convenient, high-resolution imaging method like multi-channel fNIRS may hence constitute a
57 promising approach for cognitive and clinical neuroscience that complements insights derived from
58 conventional fMRI.

59 However, the suitability of Granger-causality for analyses of hemodynamic measurements was subject
60 to controversy in the past (Friston et al., 2014; Schippers et al., 2011; Smith et al., 2012; Stokes and
61 Purdon, 2017; Webb et al., 2013; for reviews see Deshpande and Hu, 2012; Friston et al., 2013).
62 Specifically, the sampling rate of the measurement relative to the time scale of the causal mechanism
63 has been identified as a critical parameter (Deshpande et al. 2010; Barnett and Seth 2017) – an issue

64 already put forward by Granger (1969). Yet, while this constitutes a serious limitation for fMRI with
65 sampling rates of only .5-2 Hz, fNIRS samples at an order of magnitude faster. Commercially
66 available multi-channel fNIRS systems usually have sampling rates in the range of 10-250 Hz
67 (Scholkmann et al. 2014) thus providing a sufficient temporal resolution of at least 10 Hz (Roebroeck
68 et al. 2005) for estimating the directionality of influences within large-scale cortical networks.

69 The impact of physiological noise on Granger-causality inference is another potential issue of concern
70 which has previously received only little attention. Physiological noise particularly concerns analyses
71 of fNIRS data as the near-infrared light has to traverse the scalp and the skull before reaching the brain
72 and thus also samples from extra-cerebral (i.e. non-neural) tissue (Okada et al. 1997; Germon et al.
73 1999; Brigadoi and Cooper 2015). Apart from the extra-cerebral signal component, spontaneous slow
74 oscillations in the arterial blood pressure (aBP) induce autoregulatory vasomotor activity (Julien 2006)
75 and contribute to intra-cerebral signal variance in the frequency band of .1 Hz (Tong and Frederick
76 2010; Noordmans et al. 2018) commonly used for connectivity analyses (Biswal et al. 1995). Besides
77 these aBP-induced low frequency oscillations other systemic components originating from cardiac
78 pulsation, respiration and vasomotion unrelated to neural activity can bias analyses based on
79 functional measurements of brain hemodynamics (Frederick et al. 2012; Winder et al. 2017). These
80 components not only differ in their spectral properties, but also in their propagation along the
81 vasculature, i.e. they exhibit different spatiotemporal profiles (Frederick et al. 2012; Tong et al. 2012).
82 Optical measurements of blood oxygenation at the periphery (e.g. the finger) provide an easy way to
83 capture a wide spectrum of systemic hemodynamic processes and can be used to reduce physiological
84 noise in functional measurements (Frederick et al. 2012; Tong et al. 2013; Sutoko et al. 2019).

85 Analyses contrasting different conditions in a task paradigm to find cortical activations associated with
86 specific brain functions are generally assumed to be robust against extra-cerebral physiological noise
87 as well as against intra-cerebral aBP fluctuations (but see Takahashi et al., 2011). However, such
88 signal perturbations may possibly limit the reliability and validity of fNIRS-based Granger-causal
89 cross-spectral estimates of directed connectivity. More generally, any estimation of (directed as well as
90 undirected) connectivity based on hemodynamic neuroimaging such as fNIRS (but also fMRI) faces

91 the problem of distinguishing signal covariation induced by neural activity from those induced by non-
92 neural fluctuations of blood flow, blood pressure, or respiration (Tong et al. 2013; Pfurtscheller et al.
93 2017). Concerning resting-state functional connectivity estimated from hemodynamic measurements,
94 it is hence critical to minimize the impact of physiological noise and to ascertain that the measurement
95 is sensitive and specific to neural processes.

96 The present study therefore addressed the effects of physiological noise and pathological cerebral
97 hemodynamics on Granger-causal cross-spectral analyses of directed connectivity based on multi-
98 channel fNIRS data. Specifically, we investigated the influence of peripherally induced physiological
99 noise and impaired vasomotor reactivity on the reconstruction of the rostro-caudally directed
100 hierarchical organization in the PFC using a frequency-domain measure of Granger-causality (cf.
101 Schumacher et al., 2019). To this end, a sample of patients with unilateral stenosis of the internal
102 carotid artery (ICA) was assessed with fNIRS during metronomic breathing and during rest. ICA
103 stenosis leads to reduced cerebrovascular reserve capacity (Bokkers et al. 2010; Hartkamp et al. 2012),
104 impairment of cerebral autoregulation (Reinhard et al. 2003b), affects neurovascular coupling (Rossini
105 et al. 2004) and can cause cognitive impairments (Novak and Hajjar 2010; Novak 2012). As severe
106 ICA stenosis impairs cerebral autoregulation (Reinhard et al. 2003b), the hemisphere affected by ICA
107 stenosis has only limited capacity to compensate systemic low-frequency high-amplitude aBP
108 oscillations. Metronomic breathing induces strong peripheral physiological noise in terms of low-
109 frequency arterial blood pressure (aBP) oscillations that contaminate the fNIRS signal. Comparing
110 resting-state and metronomic breathing in patients with unilateral ICA stenosis thus allows
111 differentiating between the systemic effect of amplified peripheral physiological noise (i.e. aBP
112 oscillations), which contributes to both the intra- and extra-cerebral components of the fNIRS signal,
113 and the intra-cerebral effect of a compromised neurovascular system (i.e. ICA stenosis), that was
114 expected to cause differential effects of breathing-induced aBP oscillations in the patients' healthy and
115 pathological hemispheres.

116 **Methods**

117 **Patients**

118 Fifteen patients with severe unilateral stenosis or occlusion of the internal carotid artery (ICA) were
119 included and gave written informed consent prior to participation (also see Reinhard et al., 2014). The
120 advantage of using unilateral stenosis of the ICA as a quasi-experimental manipulation is that it
121 facilitates the assessment of pathological effects by comparing the affected and healthy hemisphere
122 within patients without relying on a healthy control group, yielding a higher statistical power.
123 Transcranial duplex sonography was used to determine the degree of stenosis (de Bray and Glatt 1995)
124 and the degree of intracranial collateral flow (Reinhard et al. 2003a). Magnetic resonance imaging
125 (MRI) scans were acquired from all patients and revealed a large lesion from the resection of a
126 hemangioblastoma in one patient, who was consequently excluded from the present analyses. A
127 second patient had to be excluded due to technical problems during the resting-state fNIRS
128 measurement, leaving a sample of 13 patients for analyses (mean age \pm standard deviation: 63.5 ± 10
129 years, 3 female; see Reinhard et al., 2014 for further details). The study was approved by the local
130 Ethics Committee.

131 **Data acquisition**

132 Arterial blood pressure (aBP) was continuously recorded via finger photoplethysmography (Finapres
133 2300, Ohmeda, Englewood, CO, USA) with the subject's hand positioned at heart level. Multi-channel
134 fNIRS measurements were performed using an ETG 4000 (Hitachi Medical Co., Tokyo, Japan)
135 providing 52 channels and a sampling rate of 10 Hz. In-house Matlab (version 2015a, The
136 MathWorks, Natick, MA, USA) code was used to convert the measured light absorption into
137 oxygenated and deoxygenated hemoglobin concentration changes according to the modified Lambert-
138 Beer-Law (Delpy et al. 1988). The fNIRS probes were placed on the forehead by aligning the center
139 probes with the sagittal midline and positioning the lower center probe at a distance of 1.5 cm above
140 the nasion, such that the fNIRS channels were evenly distributed across the bilateral PFC. The fNIRS
141 channel positions are illustrated in Figure 1. Patients were placed in a supine position with 50°
142 inclination of the upper body. The first measurement was conducted during a 15 minute period of rest.

143 During the second measurement patients were instructed to breath at a rate of 6 cycles/minute (i.e. .1
144 Hz) with low tidal volumes over a period of 200 s. CO₂ partial pressure was measured during
145 expiration using an infrared capnometer (Normocap©, Datex, Finland). We analyzed only the first 200
146 s of the resting state measurement, because the length of the time series potentially impacts on the
147 connectivity estimation (see below) and the direct comparison between 15 min resting state and 200 s
148 metronomic breathing would have hence been biased. However, a control analysis confirmed that
149 there were no relevant differences between 4 consecutive, 200 s long time windows of the 15 min
150 resting-state measurements (Supplementary Model S1).

151 **Data analysis**

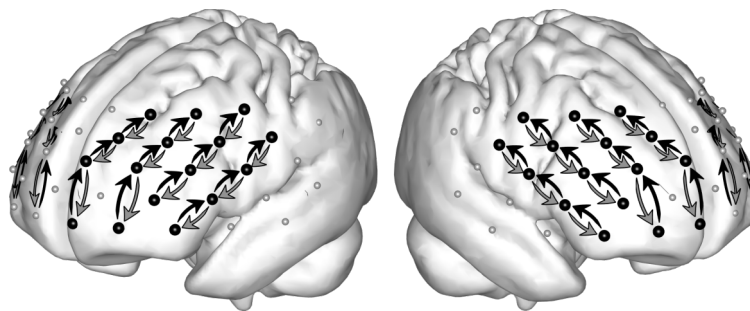
152 The aBP signal was low-pass filtered (Fourier filter, 5 Hz cutoff frequency) and downsampled to the
153 10 Hz sampling rate of the fNIRS measurement. To avoid bias of the Granger-causality estimates (see
154 below), the fNIRS data was not filtered or resampled (Florin et al. 2010; Barnett and Seth 2011).
155 However, as fNIRS is prone to movement-induced artifacts, which can cause spurious connectivity
156 (Satterthwaite et al. 2012; Santosa et al. 2017), the preprocessing requires an artifact correction step.
157 Therefore, we applied the correlation-based signal improvement (CBSI) (Cui et al. 2010), an
158 established method that effectively removes motion artifacts, increases the contrast-to-noise ratio and
159 enhances the sensitivity of the signal (Cui et al. 2010; Brigadoi et al. 2014; Racz et al. 2017;
160 Fairclough et al. 2018). It is based on the assumption that the oxygenated and the deoxygenated
161 hemoglobin concentrations are anticorrelated; as a consequence, the resulting time series of
162 oxygenated and deoxygenated hemoglobin are perfectly anticorrelated and have identical spectral
163 properties. However, the assumptions implied by the CBSI method are unlikely to be always met. We
164 therefore provide supplementary control analyses of the connectivity derived from the uncorrected
165 oxygenated and deoxygenated hemoglobin signals (Supplementary Models S2-S5). Directed
166 functional connectivity was estimated from the fNIRS measurements by directed coherence (DC)
167 (Schelter et al. 2006), a cross-spectral measure of Granger-causality, using the frequency domain
168 multivariate toolbox (www.fdm.uni-freiburg.de/Toolboxes/fdma-toolbox). As indicated by the term
169 coherence, DC is a frequency-domain measure and is calculated by fitting a vector autoregressive
170 (VAR) model, i.e. each time series is explained by its own past, as well as by the past of at least one

171 second time series using multiple lags. The series of estimated autoregression coefficients resulting
172 from the multiple lags are then transformed into the frequency domain (for details see Schelter et al.,
173 2006). Thus, DC estimated from fNIRS data represents the strength and the direction of influences
174 exerted between cortical areas in a certain frequency. For the connectivity estimates corrected for the
175 potential bias of aPB fluctuations, we included the aBP measurements in the VAR models, yielding
176 the trivariate – i.e. partial – DC (PDC). Thus, PDC estimates represent the influences between cortical
177 areas with the influences mediated by systemic physiological noise (i.e. aBP fluctuations) being
178 removed. VAR models were fitted with a model order of 20 (i.e. 20 lags), corresponding to the past 2 s
179 of the time series., The resulting model coefficients were zero-padded to the length of the time series
180 before the Fourier transformation in order to yield a smooth spectral estimate. As functional
181 connectivity is apparent in the low-frequency component of hemodynamic fluctuations (Biswal et al.
182 1995), and to cover the power peak in the fNIRS signal induced by metronomic breathing at .1 Hz, we
183 used the maximum between .06 and .12 Hz of each (P)DC spectrum for further statistical analysis. The
184 (P)DC was entered as the dependent variable in linear mixed effects models. Mixed models were fitted
185 using the lme4 package (version 1.1-14) (Bates et al. 2015) in R statistics (version 3.4.2; [http://cran.r-](http://cran.r-project.org)
186 [project.org](http://cran.r-project.org)) with unstructured variance-covariance matrices. The lmerTest package (version 2.0-33)
187 (Kuznetsova et al. 2016) was used to assess the significance of predictor terms (Type III F-statistics
188 with Satterthwaite's approximation of degrees of freedom). Post-hoc comparisons and calculation of
189 confidence intervals were performed using the lsmeans package (version 2.27-2) (Lenth 2016). As the
190 focus of the present study was on the rostro-caudal gradient of the PFC, fixed effects of all models
191 contained the factor *direction of influences*, distinguishing between influences in rostral-to-caudal and
192 caudal-to-rostral direction (Fig. 1). As recently shown (Schumacher et al. 2019), the directionality of
193 rostro-caudal functional connectivity varies across PFC regions (see also Badre and Nee, 2018;
194 Margulies et al., 2016; Nee and D'Esposito, 2016). In accordance, present models were specified with
195 a random slope allowing for varying effects of *direction* for each pair of homologues connections.
196 Additionally a random intercept for *participant* was included in each model. Fixed effect terms of each
197 model are listed in Table 1; predicted marginal means are provided in Supplementary Table 1; for
198 random effects see Supplementary Table 2.

199 **Data visualization**

200 For spatial visualization data were rendered on a standardized cortical surface derived from an
201 independent sample of healthy subjects ($n = 20$; C.P. Kaller, K. Schumacher, unpublished data). In this
202 sample, fNIRS probes were placed in the same standardized manner (see above) while location and
203 irradiation angles of fNIRS probes with respect to the subject's head were recorded using a PATRIOT
204 digitizer (Polhemus Inc., VT). Registration included recording of three fiducials (nasion, left/right
205 preauricular points) and a scattered point-wise sampling of the head surface for coregistration with
206 individual anatomical MRIs based on an iterative closest point procedure. Group averages of channel
207 positions were calculated after normalization of individual channel positions into Montreal
208 Neurological Institute (MNI) space using deformation fields derived from the segmentation of
209 anatomical MRIs with SPM8 (<http://www.fil.ion.ucl.ac.uk/spm/software/spm8/>) based on default prior
210 maps for gray and white matter and cerebrospinal fluid. A 3D Gaussian kernel with 30 mm full width
211 at half maximum was applied to render the data at the averaged channel positions on the standard
212 cortical surface (see also Schumacher et al., 2019, for further details).

213 *FI*



214 **Figure 1: Connections between fNIRS channels analyzed in the present study.** Directed connectivity between
215 neighboring channels within the PFC was analyzed along the rostro-caudal axis. Black arrows indicate rostro-
216 caudally directed connections, whereas gray arrows indicate caudo-rostrally directed connections.

217 **Results**

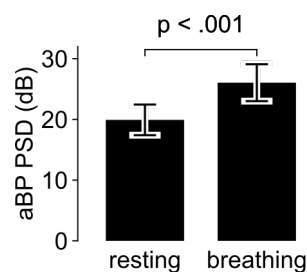
218 In the present work we analyzed the effects of amplified peripheral physiological noise (i.e. aBP
219 oscillations) and of a compromised vasomotor reactivity (i.e. ICA stenosis) on the estimation of the
220 rostro-caudally directed hierarchical organization of the PFC. Multi-channel fNIRS measurements

221 were acquired in patients with unilateral ICA stenosis during resting state and during metronomic
222 breathing at .1 Hz. Directed functional connectivity was analyzed as the dependent variable in linear
223 mixed models with a random slope allowing for varying effects of *direction* (distinguishing between
224 influences in rostral-to-caudal and caudal-to-rostral direction) for each pair of homologues connections
225 (cf. Fig. 1). Additionally a random intercept for *participant* was included in each model. The fixed
226 effects structure is described for each model in the following. An overview of the applied statistical
227 models is provided in Table 1. The predicted marginal means and corresponding confidence intervals
228 for significant effects are provided in Supplementary Table S1.

229 **Metronomic breathing increases blood pressure oscillations and overall connectivity strength**

230 As manipulation check, a one-sample t-test comparing the peak power spectral density (PSD) of the
231 continuous aBP measurement in the frequency band between .06 and .12 Hz confirmed that the
232 metronomic breathing induced strong aBP oscillations compared to the resting state (mean difference:
233 6.1 dB; $t(12) = 5.1$; $p = .0003$; Fig. 2, also see Fig. 5 for fNIRS and aBP PSD spectra).

234 *F2*

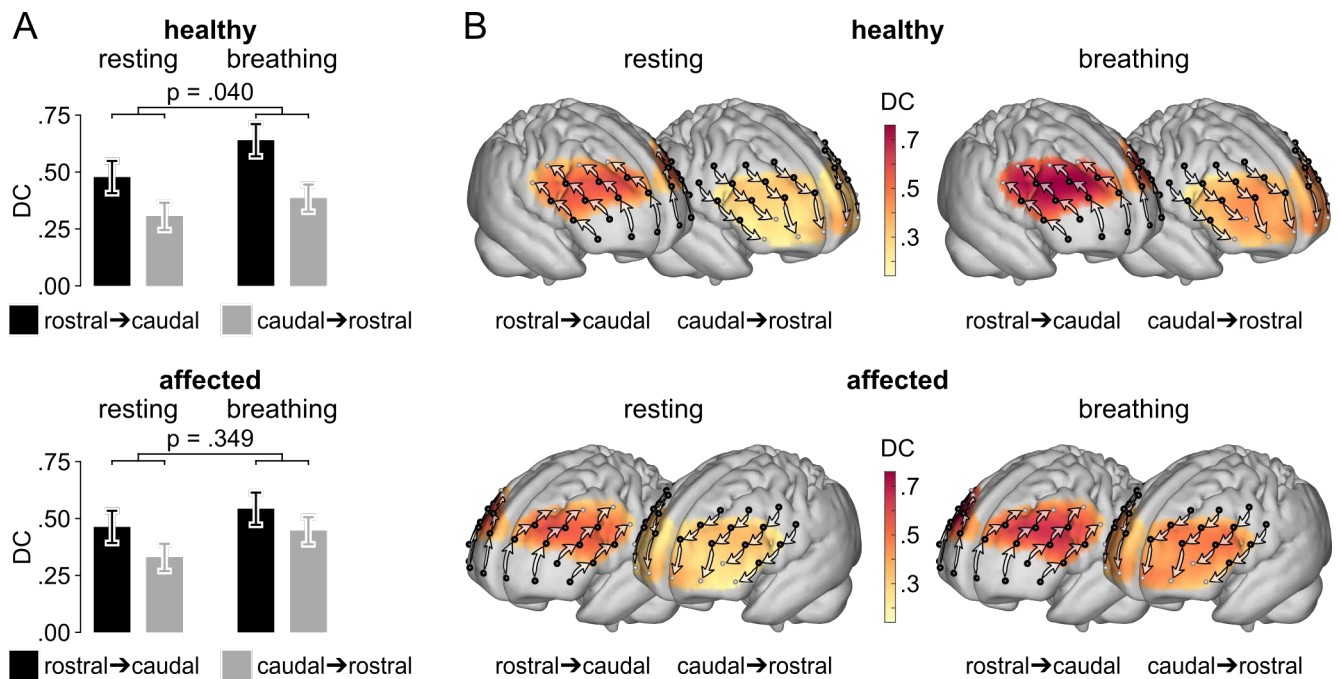


235 Figure 2: **The low-frequency power spectral density (PSD) of the arterial blood pressure (aBP) was**
236 **strongly increased during metronomic breathing compared to resting state.** Bars represent group means;
237 error bars indicate 95 % confidence intervals; p-value refers to a one-sample two-tailed t-test.

238 The first analysis of directed functional connectivity addressed the hypothesis that the impaired
239 cerebral vasomotor reactivity in the hemisphere affected by ICA stenosis would specifically attenuate
240 the rostro-caudal gradient, while the functional gradient was expected to be generally robust against
241 increased aBP oscillations induced by metronomic breathing. To this end, we fitted a linear mixed
242 model (Model 1) with a fixed effects structure comprising the three-way interaction (and all main
243 effects and lower-order interactions) between *direction* (rostro-caudal vs. caudo-rostral), *hemisphere*

244 (affected vs. healthy) and *condition* (resting state vs. metronomic breathing). The main effect for
245 *direction* confirmed the predominance of rostro-caudally directed influences ($F(1,12) = 14.6, p = .002$)
246 with higher DC estimates between adjacent fNIRS channels in rostro-caudal than in caudo-rostral
247 direction. A strong main effect for *condition* ($F(1,1212) = 61.0, p < .0001$) indicated that deep
248 breathing led to an overall increase in connectivity strength. The two-way interaction between
249 *direction* and *hemisphere* ($F(1,1212) = 12.2, p = .0005$) further indicated that ICA stenosis attenuates
250 the rostro-caudal gradient. However, the significant three-way interaction between *direction*,
251 *hemisphere*, and *condition* ($F(1,1212) = 4.5, p = .034$) revealed that the impact of breathing-induced
252 aBP oscillations on the rostro-caudal gradient was different between hemispheres (Fig. 3): The
253 difference between the directions of influences in the healthy hemisphere was larger during
254 metronomic breathing than during rest ($p = .040$) while there was no significant difference in
255 directionality between conditions in the affected hemisphere ($p = .349$). Neither the main effect for
256 *hemisphere* ($p = .642$), nor the other two-way interactions were significant (all $p > .424$). Taken
257 together, the rostro-caudal gradient in the PFC was significantly increased in the healthy hemisphere
258 by metronomic breathing while it was stable in the hemisphere affected by ICA stenosis.

259 F3



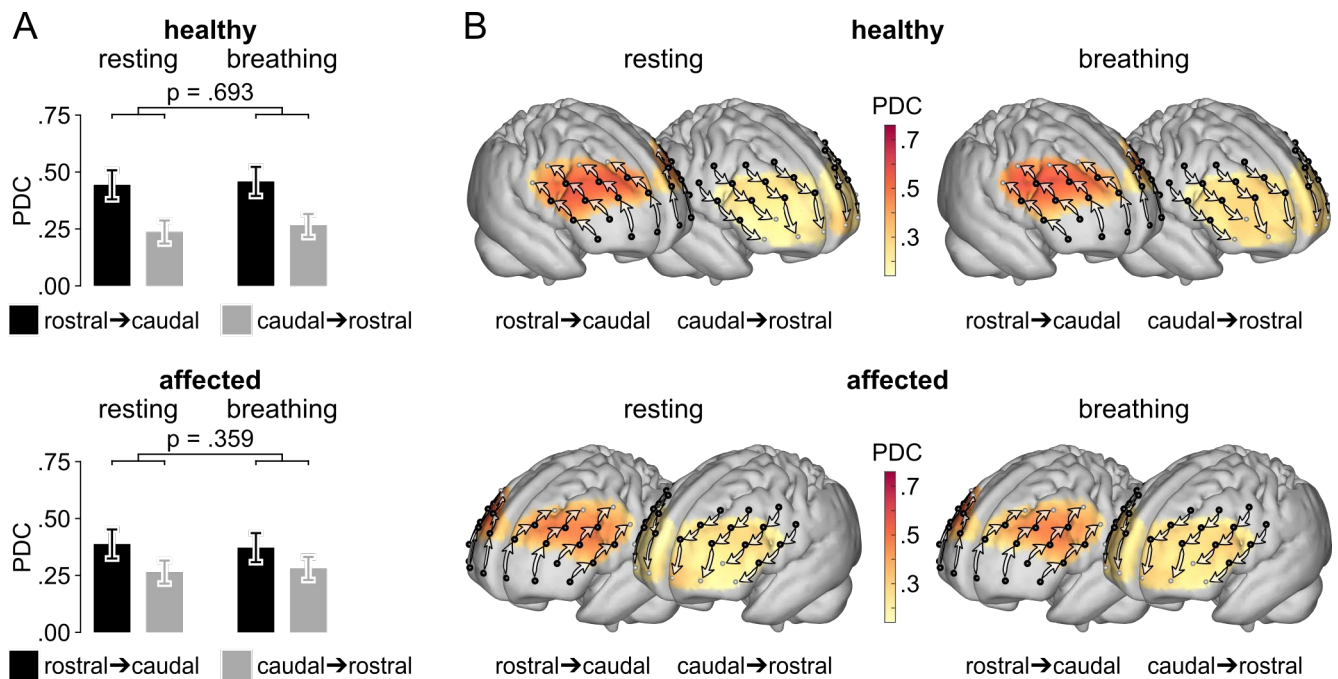
260 **Figure 3: The rostro-caudal gradient in the healthy hemisphere is increased by metronomic breathing. A:**
 261 Metronomic breathing led to an overall increase of connectivity. Moreover, rostro-caudally directed influences in
 262 the healthy hemisphere increased over-proportionally during metronomic breathing (Model 1). As shown in
 263 Figure 4, this difference between conditions disappeared after intra-individually adjusting the estimation of
 264 directed connectivity for aBP oscillations, whereas the difference between the healthy and affected hemisphere
 265 was preserved. $N = 13$; bars represent least square means; error bars indicate 95 % confidence intervals. **B:**
 266 Topographic illustration of the connectivity estimates, representing the influences from channels (black dots)
 267 toward caudally (left brain) and rostrally (right brain) neighboring channels as indicated by arrows; darker red
 268 colors signify stronger influences. Data for patients with stenosis of the right ICA were flipped such that the
 269 affected side is represented on the left hemisphere.

270 **Adjusting estimates of directed connectivity for arterial blood pressure oscillations (intra-** 271 **individual approach)**

272 As metronomic breathing not only caused a marked increase in overall connectivity strength but also
 273 changed the rostro-caudal gradient in the healthy hemisphere we sought to intra-individually control
 274 for the potentially underlying mediation effect of aBP oscillations in a second analysis. To this end, we
 275 calculated the trivariate – i.e. partial – DC (PDC) between each fNIRS channel pair and the continuous
 276 aBP time series at the level of the individual subject, thereby removing estimated influences between
 277 brain regions that were mediated by aBP oscillations. The linear mixed model with the factors
 278 *direction*, *hemisphere*, and *condition* (as specified above) was fitted to these aBP-corrected

279 connectivity estimates (Model 2) and demonstrated that changes induced by metronomic breathing
280 were entirely mediated by aBP oscillations: Neither the main effect for *condition* ($p = .377$), nor any
281 interaction involving *condition* was significant in the model fitted to the aBP-corrected data (all $p >$
282 $.354$; see Table 1). However, main effects for *direction* ($F(1,12) = 19.8, p = .0007$) and *hemisphere*
283 ($F(1,1223) = 4.0, p = .044$) as well as their interaction ($F(1,1223) = 14.5, p = .0001$) were significant.
284 Thus, intra-individually adjusting for effects of aBP oscillations not only allowed to correct breathing
285 induced artificial increases in the magnitudes of estimates of directed connectivity, but also revealed
286 that the connectivity gradient in the stenosed compared to the healthy hemisphere was generally
287 attenuated irrespective of the condition (breathing vs. rest).

288 In order to explicitly test the effects of correcting the connectivity for aBP oscillations, supplementary
289 analyses directly compared the uncorrected DC estimates and the aBP-corrected PDC estimates
290 (Supplementary Model S6 and S7). These analyses confirmed that (i) the general over-estimation of
291 connectivity strength in both hemispheres and (ii) the increased rostro-caudal gradient in the healthy
292 hemisphere caused by metronomic breathing disappeared after correcting for aBP oscillations.

293 *F4*

294 Fig 4: Including the aBP time series in the connectivity estimation entirely removed the effect of
 295 metronomic breathing on the rostro-caudal connectivity. **A:** The effect that metronomic breathing exerted on
 296 the connectivity estimates was adjusted by including the aBP time series into the VAR model. This correction
 297 preserved the difference between hemispheres and revealed that the attenuation of the rostro-caudal gradient by
 298 ICA stenosis was independent of aBP fluctuations but reflected the compromised integrity of the functional
 299 network. P-values were obtained by fitting Model 1 (Figure 3) to the aBP-corrected connectivity estimates
 300 (Model 2). $N = 13$; bars represent least square means; error bars indicate 95 % confidence intervals. **B:**
 301 Topographic illustration of the aBP-corrected connectivity estimates, representing the influences from channels
 302 (black dots) toward caudally (left brain) and rostrally (right brain) neighboring channels as indicated by arrows;
 303 darker red colors signify stronger influences. Data for patients with stenosis of the right ICA were flipped such
 304 that the affected side is represented on the left hemisphere.

305 Although the CBSI method used in the present analyses to improve signal quality is an established
 306 method that has been validated and compared to other artifact correction methods multiple times (e.g.
 307 Cooper et al. 2012; Brigadoi et al. 2014; Racz et al. 2017; Mukli et al. 2018; Fairclough et al. 2018;
 308 Fishburn et al. 2019), a systematic analysis of the impact of the CBSI method on Granger causality
 309 inference has not been performed yet. We therefore conducted control analyses on the uncorrected
 310 deoxygenated (dxyHb) and oxygenated (oxyHb) hemoglobin data (Supplementary Model S2-S5). The
 311 resulting connectivity estimates are depicted in Supplementary Figure S1 (DC) and S2 (PDC,
 312 corrected for influences by aBP fluctuations). In brief, the pattern of DC estimates, derived from the

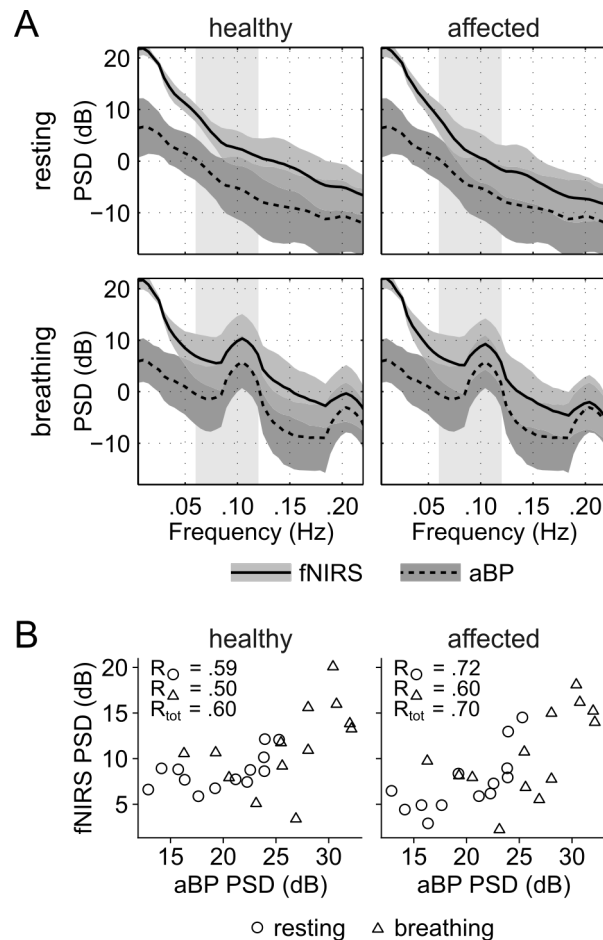
oxyHb data markedly deviated from those derived from the CBSI data, while the dxyHb-derived connectivity pattern was similar to the CBSI-derived pattern. Furthermore, the PDC estimates (i.e. the connectivity corrected for aBP influences) were similar for the oxyHb, dxyHb, and CBSI data suggesting that the deviating results for the oxyHb-derived DC estimates were due to the higher susceptibility of the oxyHb measurement to physiological noise as previously reported (Obrig et al. 2000; Zhang et al. 2009; Kirilina et al. 2012; Sutoko et al. 2019). This again corroborates our finding that including the aBP signal in PDC estimation effectively controlled for bias induced by physiological noise.

Low-frequency aBP variance is reflected in low-frequency fNIRS variance

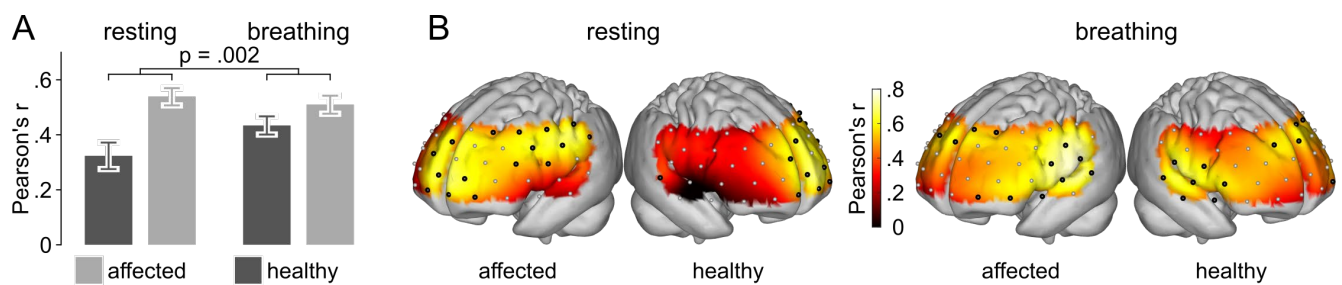
The strong intra-individual effect of including peripheral measured aBP oscillations in the PDC estimation of the directed functional connectivity raises the question whether the magnitude of the aBP oscillations is reflected in the low-frequency component of the fNIRS signal. Correlations between the peak power spectral density (PSD, in dB) of the peripheral aBP and the fNIRS signals in the frequency band between .06 and .12 Hz (Fig. 5a) revealed strong associations between the low-frequency variance of the aBP and the fNIRS signals across patients (Fig. 5b). The spatial distribution of correlation coefficients (Fig. 6b) indicated considerable variation across hemispheres and conditions. A 2×2 repeated measures analysis of variance (ANOVA; performed using the ez package for R, version 4.4-0; Lawrence, 2016) on the fisher-transformed Pearson correlation coefficients (Model 3, calculated with the homologous channels as the unit of observation) showed that correlations were stronger in the affected than in the healthy hemisphere ($F(1,15) = 11.63$, $p = .004$, generalized $\eta^2 = .194$; Fig. 6a). Furthermore, the significant interaction effect between *hemisphere* and *condition* ($F(1,15) = 13.40$, $p = .002$, generalized $\eta^2 = .043$) revealed that the correlation difference between conditions was mainly driven by elevated PSD correlations in the healthy hemisphere during metronomic breathing compared to resting state (mean difference: .122, $t(15) = 1.72$, $p = .11$); the difference between conditions in the affected hemisphere was considerably smaller (mean difference: .035, $t(15) = .568$, $p = .58$). These effects clearly demonstrate the impairment of the vasomotor reactivity in the stenosed hemisphere (where aBP fluctuations appeared almost undamped), not only during metronomic breathing but also during rest. Averaged across channels and conditions, the low-

341 frequency PSD of the fNIRS signal shared 23% of variance with the low-frequency PSD of the
 342 peripheral aBP (Fig. 5b).

343 *F5*



344 **Fig. 5: The power spectral density (PSD) of the fNIRS signal and the continuously measured aBP.** **A:** PSD
 345 of the fNIRS (solid line) and the aBP (dashed line) signals during resting state (top panels) and metronomic
 346 breathing (bottom panels) separately for the healthy and the stenosed hemisphere. The aBP was measured by a
 347 finger plethysmograph and its PSD is shown twice along with the fNIRS PSD for both hemispheres to facilitate
 348 comparison. The fNIRS PSDs were averaged across channels within each hemisphere; lines represent averages
 349 across patients and gray patches indicate standard deviations across patients. The area shaded in light gray marks
 350 the frequency band between .06 and .12 Hz which was used for analyses. **B:** Scatter plot of aBP and fNIRS
 351 PSDs. From each PSD spectrum the maximum in the frequency band of interest was used. The fNIRS PSD
 352 values were averaged across channels included in the mixed model analyses. The correlations between PSDs for
 353 single fNIRS channels are shown topographically in Figure 6b.

354 *F6*

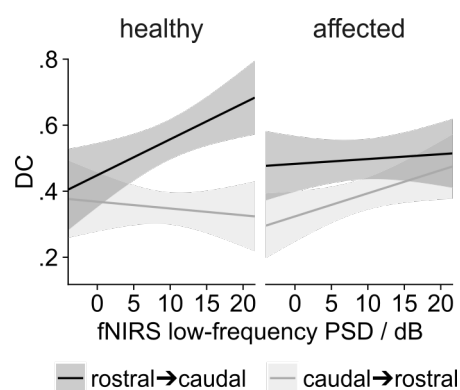
355 **Fig 6: The coupling between low-frequency aBP and fNIRS signal variance in the healthy hemisphere is**
 356 **increased by metronomic breathing.** **A:** The correlations between the peak PSD in the frequency band [.06
 357 .12] Hz of the aBP and each fNIRS channel were calculated, Fisher-Z-transformed, and analyzed in a repeated
 358 measures ANOVA (Model 3). In the resting state the impairment of the vasomotor reactivity by the ICA stenosis
 359 caused high correlations between aBP and fNIRS PSDs in the affected hemisphere, which were not further
 360 increased by metronomic breathing. In contrast, the vasculature of the healthy hemisphere with its intact
 361 autoregulation minimized PSD correlations in the resting state. However, metronomic breathing induced strong
 362 aBP oscillations also in the healthy hemisphere which lead to a marked increase in PSD correlations. Taken
 363 together, coupling between aBP and fNIRS signal variance increased by metronomic breathing in the healthy but
 364 not in the stenosed hemisphere. $N = 13$; bars represent mean correlation coefficients; error bars indicate standard
 365 error of the mean. **B:** Topographic illustration of correlation coefficients. Black dots mark channels for which
 366 correlation was significant ($p < .05$, uncorrected). For the sake of completeness, this figure shows correlations
 367 for all fNIRS channels, i.e. also for those not included in the connectivity analyses, while the ANOVA
 368 considered only channels that contributed to at least one connection (cf. Fig. 1). Data for patients with stenosis of
 369 the right ICA were flipped such that the affected side is represented on the left hemisphere.

370 **Low-frequency fNIRS-variance accounts for the effect of metronomic breathing (inter-** 371 **individual approach)**

372 Given the strong association between the low-frequency variation in the aBP and the fNIRS signals
 373 across patients, we further asked whether the fNIRS PSD can serve as a proxy for the intra-individual
 374 aBP fluctuations in order to explain the effect of breathing on estimates of directed connectivity on the
 375 inter-individual level. As this could provide a general possibility to correct the connectivity estimates
 376 for the aBP induced bias without relying on monitoring the peripheral aBP time course, we tested
 377 whether the low-frequency fNIRS PSD can account for aBP-induced variance in the connectivity
 378 estimates. Accordingly, the first model (using the uncorrected connectivity estimates) was extended by
 379 the peak PSD of the fNIRS signals in the frequency band between .06 and .12 Hz as a covariate,
 380 including all resulting 2-, 3- and 4-way interactions with the nominal predictors (Model 4). As there is

381 one peak PSD value for each fNIRS channel, we used the mean value of the respective channel pairs
 382 for the corresponding connections. In addition to main effects for *direction* ($F(1,28.0) = 4.5, p = .042$)
 383 and *condition* ($F(1,1028) = 6.2, p = .013$), this model revealed a simple effect of the continuous
 384 predictor *low-frequency PSD* ($F(1,224.8) = 6.2, p = .014$). As expected, the 2-way interaction between
 385 *direction* and *hemisphere* ($F(1,1207.1) = 1.4, p = .234$) and, more importantly, the 3-way interaction
 386 between *direction*, *hemisphere*, and *condition* ($F(1,1205.9) = .9, p = .340$) disappeared. Instead, the
 387 significant 3-way interaction between *direction*, *hemisphere*, and *low-frequency PSD* ($F(1,1207.3) =$
 388 $7.8, p = .005$) revealed a positive correlation between the rostro-caudal gradient and the variance in the
 389 low-frequency fNIRS signal component in the healthy hemisphere only (Fig. 7, left panel; contrast
 390 between slopes for *low-frequency PSD* of rostrally and caudally directed influences in the healthy
 391 hemisphere: $p = .008$). In the affected hemisphere, *low-frequency PSD* did not predict the difference
 392 between rostrally and caudally directed influences ($p = .239$). Thus, the low-frequency variance of the
 393 fNIRS signal (i) moderated the effect of *hemisphere* (i.e. of the ICA stenosis) on the rostro-caudal
 394 gradient and (ii) mediated the effect of *condition* (i.e. of aBP oscillations) on the gradient in the
 395 healthy hemisphere. No further effects were significant (all $p > .198$).

396 *F7*



397 **Fig 7: The fNIRS signal power explained variance in the connectivity estimates in the healthy hemisphere.**
 398 The low-frequency power spectral density (PSD) of the fNIRS signals mediated the effect of *condition* on the
 399 rostro-caudal gradient, i.e. the effect of *condition* (Fig. 3) disappeared after including the fNIRS PSD as a
 400 predictor in the linear mixed model (Model 4). $N = 13$; model predictions are shown with 95% non-simultaneous
 401 confidence bands.

402 *TI*403 Table 1: **Type III statistics for second-level models**

| Model (Figures) | Effect | df | Error df | F value | p value |
|--|---|-----------|-----------------|----------------|---------------------------------------|
| Model 1 DC LMM (Figure 3) | direction | 1 | 12 | 14.57 | .0025 |
| | condition | 1 | 1212 | 60.97 | 1×10^{-14} |
| | hemisphere | 1 | 1212 | .22 | .6419 |
| | direction \times condition | 1 | 1212 | .63 | .4292 |
| | direction \times hemisphere | 1 | 1212 | 12.20 | .0005 |
| | condition \times hemisphere | 1 | 1212 | .64 | .4250 |
| | direction \times condition \times hemisphere | 1 | 1212 | 4.48 | .0345 |
| Model 2 PDC LMM (aBP corrected connectivity; Figure 4) | direction | 1 | 12 | 19.79 | .0008 |
| | condition | 1 | 1223 | .78 | .3767 |
| | hemisphere | 1 | 1223 | 4.05 | .0444 |
| | direction \times condition | 1 | 1223 | .86 | .3537 |
| | direction \times hemisphere | 1 | 1223 | 14.49 | .0001 |
| | condition \times hemisphere | 1 | 1223 | .79 | .3741 |
| | direction \times condition \times hemisphere | 1 | 1223 | .14 | .7117 |
| Model 3 ANOVA of PSD correlations (Figure 6) | condition | 1 | 15 | .47 | .5027 |
| | hemisphere | 1 | 15 | 11.63 | .0039 |
| | condition \times hemisphere | 1 | 15 | 13.40 | .0023 |
| Model 4 DC LMM with fNIRS PSD covariate (Figure 7) | dir | 1 | 28 | 4.54 | .0419 |
| | condition | 1 | 1028 | 6.17 | .0132 |
| | hemisphere | 1 | 1230 | .00 | .9591 |
| | PSD _{fNIRS} | 1 | 225 | 6.16 | .0138 |
| | direction \times condition | 1 | 1206 | .21 | .6451 |
| | direction \times hemisphere | 1 | 1207 | 1.41 | .2345 |
| | condition \times hemisphere | 1 | 1225 | 1.40 | .2369 |
| | direction \times PSD _{fNIRS} | 1 | 1211 | 1.66 | .1982 |
| | condition \times PSD _{fNIRS} | 1 | 1040 | .05 | .8242 |
| | hemisphere \times PSD _{fNIRS} | 1 | 1233 | .06 | .8047 |
| | direction \times condition \times hemisphere | 1 | 1206 | .91 | .3402 |
| | direction \times condition \times PSD _{fNIRS} | 1 | 1207 | .47 | .4933 |
| | direction \times hemisphere \times PSD _{fNIRS} | 1 | 1207 | 7.83 | .0052 |
| | condition \times hemisphere \times PSD _{fNIRS} | 1 | 1228 | .86 | .3544 |
| direction \times condition \times hemisphere \times PSD _{fNIRS} | 1 | 1206 | .32 | .5746 | |

404 NB: Tests of linear mixed models (LMM) were performed using the lmerTest package (Kuznetsova et al. 2016),
405 with Satterthwaite approximation of degrees of freedom. Abbreviations: ANOVA, analysis of variance; DC,
406 directed coherence; df, degrees of freedom; LMM, linear mixed model; PDC, partial directed coherence; PSD,
407 power spectral density (in the low frequency band).

408 Discussion

409 The present study addressed effects of physiological noise and vasomotor reactivity on Granger-causal
410 cross-spectral analyses of multi-channel fNIRS data with high temporal resolution. Specifically, we

411 asked (i) whether physiological noise, which inevitably contaminates fNIRS measurements, biases
412 Granger-causality estimates of directed connectivity along the rostral-caudal axis in the PFC, and (ii)
413 whether severe carotid artery stenosis, which impairs the neurovascular coupling in the PFC (Rossini
414 et al. 2004; Bokkers et al. 2010; Novak and Hajjar 2010; Hartkamp et al. 2012; Novak 2012) also
415 affects the rostral-caudal hierarchical organization of the PFC. We found that the impact of strong aBP
416 oscillations on the directed connectivity estimates was direction-unspecific and could be removed by
417 including the aBP time course in the connectivity estimation. Additionally, the effect of aBP
418 oscillations on the directed functional connectivity was explained by the low-frequency power of the
419 fNIRS signal. Furthermore, results showed that the rostral-caudal functional organization of the PFC in
420 the affected hemisphere was specifically attenuated by ICA stenosis. Taken together, Granger-causal
421 cross-spectral analyses of resting-state fNIRS measurements were robust against ordinary levels of
422 physiological noise but sensitive to the integrity of the neurovascular system.

423 The enhancing effect of the breathing-induced fNIRS signal oscillations on the connectivity estimates
424 demonstrated that the manipulation of this physiological parameter biased the estimation of directed
425 connectivity. As it is very unlikely that this change in connectivity reflects a change in functional
426 organization evoked by the instruction of metronomic breathing, the increased low-frequency signal
427 variance (at .1 Hz) probably caused elevated estimates of functional connections. This interpretation is
428 supported by three observations: (i) The increase in connectivity during metronomic breathing was
429 more pronounced in the healthy compared to the stenosed hemisphere. As ICA stenosis caused a
430 reduction of the vasomotor reactivity and impaired the cerebral autoregulation in the affected
431 hemisphere (Bokkers et al. 2010; Reinhard et al. 2014), the vasculature had less capacity to
432 compensate aBP fluctuations, presumably already in the resting state. Thus, the coupling between aBP
433 and the fNIRS signal was increased by metronomic breathing only in the healthy but not in the
434 stenosed hemisphere (Fig. 6) and, accordingly, exerted a stronger effect on estimates of directed
435 connectivity in the healthy than in the stenosed hemisphere. (ii) The effect of breathing-induced
436 increases of directed connectivity completely disappeared after including the aBP signal (the
437 continuous finger photoplethysmogram measurements) in the intra-individual connectivity estimation.
438 The change in connectivity between resting and breathing condition was thus entirely explained by

439 systemic aBP fluctuations (i.e. non-neural signal variance). (iii) Besides the peripheral, global
440 hemodynamic signal, the local, low-frequency power spectral density of the fNIRS time series also
441 reflected the effect of metronomic breathing on the connectivity, i.e. the low-frequency power spectral
442 density accounted for the difference between conditions. The fact that the connectivity gradient was
443 predicted by the low-frequency signal variance only in the healthy and not in the affected hemisphere
444 indicates that strong vasomotion can bias the Granger-causal estimates of directed connectivity. Taken
445 together, we conclude that the impact of peripheral physiological parameters, notably aBP oscillations,
446 on Granger-causality inference can be adjusted by taking inter-individual differences in fNIRS signal
447 variance into account. However, when comparing connectivity estimated from measurements under
448 conditions with considerable variations in aBP, the present results advise to include the aBP time
449 series in the intra-individual connectivity estimation in order to preclude that differences in
450 connectivity are caused simply by autoregulatory vasomotion. In this respect, it is worth noting that
451 peripheral photoplethysmography used to measure slow aBP fluctuations in the present study also
452 capture cardiac and respiratory pulsations, which have been shown to constitute noise sources in
453 functional hemodynamic measurements as well (Frederick et al. 2012). Thus, improvement of
454 connectivity estimates by including the aBP time-series in the VAR model may have also relied on the
455 suppression of other systemic physiological noise sources.

456 In contrast to the effect of metronomic breathing, the effect of ICA stenosis on the connectivity
457 estimates was persistent after correcting for the global hemodynamic component as well as after taking
458 the local signal variance into account. The difference in connectivity between healthy and affected
459 hemisphere therefore reflected the integrity of the functional network organization rather than mere
460 physiological processes. This finding was highly expected as ICA stenosis has been shown before not
461 only to impair the hemodynamic response (Rossini et al. 2004) and functional connectivity (Avirame
462 et al. 2015) but also to cause functional deficits like cognitive decline (Novak and Hajjar 2010; Novak
463 2012). However, as no behavioral data were available for the present sample of patients, the
464 relationship between alterations in the rostro-caudal connectivity gradient and specific cognitive
465 function requires further research. Moreover, future studies should take advantage of more recent
466 advancements in fNIRS technology and, specifically, capitalize on multi-distance and tomographic

467 measurements to more efficiently eliminate extra-cerebral signal components (Habermehl et al. 2012;
468 Eggebrecht et al. 2014; Gagnon et al. 2014; Sato et al. 2016).

469 In summary, the high temporal resolution of fNIRS renders Granger-causality analyses of
470 hemodynamic measurements possible and allows the comparison of different conditions provided that
471 physiological parameters like aBP are controlled. In line with previous studies we demonstrated that
472 (i) peripheral measurements of systemic hemodynamic processes can be used to correct functional
473 connectivity estimates for physiological noise (Frederick et al. 2012; Tong et al. 2013; Sutoko et al.
474 2019) and that (ii) ICA stenosis impairs functional network organization (Avirame et al. 2015).

475 **References**

476 Avirame K, Lesemann A, List J, et al (2015) Cerebral autoregulation and brain networks in occlusive
477 processes of the internal carotid artery. *J Cereb Blood Flow Metab* 35:240–247. doi:
478 10.1038/jcbfm.2014.190

479 Badre D, D’Esposito M (2007) Functional magnetic resonance imaging evidence for a hierarchical
480 organization of the prefrontal cortex. *J Cogn Neurosci* 19:2082–2099

481 Badre D, Nee DE (2018) Frontal Cortex and the Hierarchical Control of Behavior. *Trends Cogn Sci*
482 22:170–188. doi: 10.1016/j.tics.2017.11.005

483 Barnett L, Seth AK (2017) Detectability of Granger causality for subsampled continuous-time
484 neurophysiological processes. *J Neurosci Methods* 275:93–121. doi:
485 10.1016/j.jneumeth.2016.10.016

486 Barnett L, Seth AK (2011) Behaviour of Granger causality under filtering: theoretical invariance and
487 practical application. *J Neurosci Methods* 201:404–19. doi: 10.1016/j.jneumeth.2011.08.010

488 Bates D, Mächler M, Bolker B, Walker S (2015) Fitting Linear Mixed-Effects Models Using lme4. *J*
489 *Stat Softw* 67:1–48. doi: 10.18637/jss.v067.i01

490 Biswal B, Yetkin FZ, Haughton VM, Hyde JS (1995) Functional connectivity in the motor cortex of

- 491 resting human brain using echo-planar MRI. *Magn Reson Med* 34:537–41. doi:
492 10.1002/mrm.1910340409
- 493 Blumenfeld RS, Nomura EM, Gratton C, D’Esposito M (2013) Lateral prefrontal cortex is organized
494 into parallel dorsal and ventral streams along the rostro-caudal axis. *Cereb Cortex* 23:2457–66.
495 doi: 10.1093/cercor/bhs223
- 496 Bokkers RPH, van Osch MJP, van der Worp HB, et al (2010) Symptomatic carotid artery stenosis:
497 impairment of cerebral autoregulation measured at the brain tissue level with arterial spin-
498 labeling MR imaging. *Radiology* 256:201–8. doi: 10.1148/radiol.10091262
- 499 Brigadoi S, Ceccherini L, Cutini S, et al (2014) Motion artifacts in functional near-infrared
500 spectroscopy: A comparison of motion correction techniques applied to real cognitive data.
501 *Neuroimage* 85:181–191. doi: 10.1016/j.neuroimage.2013.04.082
- 502 Brigadoi S, Cooper RJ (2015) How short is short? Optimum source-detector distance for short-
503 separation channels in functional near-infrared spectroscopy. *Neurophotonics* 2:025005. doi:
504 10.1117/1.NPh.2.2.025005
- 505 Christoff K, Gabrieli JDE (2000) The frontopolar cortex and human cognition: Evidence for a
506 rostrocaudal hierarchical organization within the human prefrontal cortex. *Psychobiology*
507 28:168–186
- 508 Cooper RJ, Selb J, Gagnon L, et al (2012) A Systematic Comparison of Motion Artifact Correction
509 Techniques for Functional Near-Infrared Spectroscopy. *Front Neurosci* 6:1–10. doi:
510 10.3389/fnins.2012.00147
- 511 Cui X, Bray S, Reiss AL (2010) Functional near infrared spectroscopy (NIRS) signal improvement
512 based on negative correlation between oxygenated and deoxygenated hemoglobin dynamics.
513 *Neuroimage* 49:3039–46. doi: 10.1016/j.neuroimage.2009.11.050
- 514 de Bray JM, Glatt B (1995) Quantification of Atheromatous Stenosis in the Extracranial Internal
515 Carotid Artery. *Cerebrovasc Dis* 5:414–426. doi: 10.1159/000107895

- 516 Delpy DT, Cope M, van der Zee P, et al (1988) Estimation of optical pathlength through tissue from
517 direct time of flight measurement. *Phys Med Biol* 33:1433–42
- 518 Deshpande G, Hu X (2012) Investigating effective brain connectivity from fMRI data: past findings
519 and current issues with reference to Granger causality analysis. *Brain Connect* 2:235–245. doi:
520 10.1089/brain.2012.0091 [doi]
- 521 Deshpande G, Sathian K, Hu X (2010) Effect of hemodynamic variability on Granger causality
522 analysis of fMRI. *Neuroimage* 52:884–896. doi: 10.1016/j.neuroimage.2009.11.060
- 523 Eggebrecht AT, Ferradal SL, Robichaux-Viehoever A, et al (2014) Mapping distributed brain function
524 and networks with diffuse optical tomography. *Nat Photonics* 8:448–454. doi:
525 10.1038/nphoton.2014.107
- 526 Fairclough SH, Burns C, Kreplin U (2018) FNIRS activity in the prefrontal cortex and motivational
527 intensity: impact of working memory load, financial reward, and correlation-based signal
528 improvement. *Neurophotonics* 5:035001. doi: 10.1117/1.NPh.5.3.035001
- 529 Fishburn FA, Ludlum RS, Vaidya CJ, Medvedev A V. (2019) Temporal Derivative Distribution
530 Repair (TDDR): A motion correction method for fNIRS. *Neuroimage* 184:171–179. doi:
531 10.1016/j.neuroimage.2018.09.025
- 532 Florin E, Gross J, Pfeifer J, et al (2010) The effect of filtering on Granger causality based multivariate
533 causality measures. *Neuroimage* 50:577–588. doi:
534 <http://dx.doi.org/10.1016/j.neuroimage.2009.12.050>
- 535 Frederick B deB, Nickerson LD, Tong Y (2012) Physiological denoising of BOLD fMRI data using
536 Regressor Interpolation at Progressive Time Delays (RIPTiDe) processing of concurrent fMRI
537 and near-infrared spectroscopy (NIRS). *Neuroimage* 60:1913–23. doi:
538 10.1016/j.neuroimage.2012.01.140
- 539 Friston K, Moran R, Seth AK (2013) Analysing connectivity with Granger causality and dynamic
540 causal modelling. *Curr Opin Neurobiol* 23:172–8. doi: 10.1016/j.conb.2012.11.010

- 541 Friston KJ, Bastos AM, Oswal A, et al (2014) Granger causality revisited. *Neuroimage* 101:796–808.
542 doi: 10.1016/j.neuroimage.2014.06.062
- 543 Fuster JM (2008) *The Prefrontal Cortex*, 4th edn. Academic Press/Elsevier, London
- 544 Gagnon L, Yücel M a., Boas D a., Cooper RJ (2014) Further improvement in reducing superficial
545 contamination in NIRS using double short separation measurements. *Neuroimage* 85:127–135.
546 doi: 10.1016/j.neuroimage.2013.01.073
- 547 Germon TJ, Evans PD, Barnett NJ, et al (1999) Cerebral near infrared spectroscopy: emitter-detector
548 separation must be increased. *Br J Anaesth* 82:831–837
- 549 Granger CWJ (1969) Investigating Causal Relations by Econometric Models and Cross-spectral
550 Methods. *Econometrica* 37:424. doi: 10.2307/1912791
- 551 Habermehl C, Holtze S, Steinbrink J, et al (2012) Somatosensory activation of two fingers can be
552 discriminated with ultrahigh-density diffuse optical tomography. *Neuroimage* 59:3201–11. doi:
553 10.1016/j.neuroimage.2011.11.062
- 554 Hartkamp NS, Hendrikse J, van der Worp HB, et al (2012) Time Course of Vascular Reactivity Using
555 Repeated Phase-Contrast MR Angiography in Patients With Carotid Artery Stenosis. *Stroke*
556 43:553–556. doi: 10.1161/STROKEAHA.111.637314
- 557 Julien C (2006) The enigma of Mayer waves: Facts and models. *Cardiovasc Res* 70:12–21. doi:
558 10.1016/j.cardiores.2005.11.008
- 559 Kirilina E, Jelzow A, Heine A, et al (2012) The physiological origin of task-evoked systemic artefacts
560 in functional near infrared spectroscopy. *Neuroimage* 61:70–81. doi:
561 10.1016/j.neuroimage.2012.02.074
- 562 Koechlin E, Ody C, Kouneiher F (2003) The architecture of cognitive control in the human prefrontal
563 cortex. *Science* 302:1181–5. doi: 10.1126/science.1088545
- 564 Kuznetsova A, Bruun Brockhoff P, Haubo Bojesen Christensen R (2016) lmerTest: Tests in Linear

565 Mixed Effects Models

566 Lawrence MA (2016) ez: Easy Analysis and Visualization of Factorial Experiments

567 Lenth R V (2016) Least-Squares Means: The R Package lsmeans. *J Stat Softw* 69:1–33. doi:
568 10.18637/jss.v069.i01

569 Mader W, Feess D, Lange R, et al (2008) On the Detection of Direct Directed Information Flow in
570 fMRI. *IEEE J Sel Top Signal Process* 2:965–974. doi: 10.1109/JSTSP.2008.2008260

571 Margulies DS, Ghosh SS, Goulas A, et al (2016) Situating the default-mode network along a principal
572 gradient of macroscale cortical organization. *Proc Natl Acad Sci U S A* 113:12574–12579. doi:
573 10.1073/pnas.1608282113

574 Mukli P, Nagy Z, Racz FS, Eke HP (2018) Impact of Healthy Aging on Multifractal Hemodynamic
575 Fluctuations in the Human Prefrontal Cortex. *Front Physiol* 9:1072. doi:
576 10.3389/fphys.2018.01072

577 Nee DE, D’Esposito M (2016) The hierarchical organization of the lateral prefrontal cortex. *Elife* 5:1–
578 26. doi: 10.7554/eLife.12112

579 Noordmans HJ, van Blooijis D, Siero JCW, et al (2018) Detailed view on slow sinusoidal,
580 hemodynamic oscillations on the human brain cortex by Fourier transforming oxy/deoxy
581 hyperspectral images. *Hum Brain Mapp* 39:3558–3573. doi: 10.1002/hbm.24194

582 Novak V (2012) Cognition and Hemodynamics. *Curr Cardiovasc Risk Rep* 6:380–396. doi:
583 10.1007/s12170-012-0260-2

584 Novak V, Hajjar I (2010) The relationship between blood pressure and cognitive function. *Nat Rev*
585 *Cardiol* 7:686–98. doi: 10.1038/nrcardio.2010.161

586 Obrig H, Neufang M, Wenzel R, et al (2000) Spontaneous low frequency oscillations of cerebral
587 hemodynamics and metabolism in human adults. *Neuroimage* 12:623–39. doi:
588 10.1006/nimg.2000.0657

- 589 Okada E, Firbank M, Schweiger M, et al (1997) Theoretical and experimental investigation of near-
590 infrared light propagation in a model of the adult head. *Appl Opt* 36:21–31
- 591 Pfurtscheller G, Schwerdtfeger A, Brunner C, et al (2017) Distinction between Neural and Vascular
592 BOLD Oscillations and Intertwined Heart Rate Oscillations at 0.1 Hz in the Resting State and
593 during Movement. *PLoS One* 12:e0168097. doi: 10.1371/journal.pone.0168097
- 594 Racz FS, Mukli P, Nagy Z, Eke A (2017) Increased prefrontal cortex connectivity during cognitive
595 challenge assessed by fNIRS imaging. *Biomed Opt Express* 8:3842–3855. doi:
596 10.1364/BOE.8.003842
- 597 Reinhard M, Müller T, Guschlbauer B, et al (2003a) Dynamic cerebral autoregulation and collateral
598 flow patterns in patients with severe carotid stenosis or occlusion. *Ultrasound Med Biol*
599 29:1105–1113. doi: 10.1016/S0301-5629(03)00954-2
- 600 Reinhard M, Roth M, Müller T, et al (2003b) Cerebral autoregulation in carotid artery occlusive
601 disease assessed from spontaneous blood pressure fluctuations by the correlation coefficient
602 index. *Stroke* 34:2138–44. doi: 10.1161/01.STR.0000087788.65566.AC
- 603 Reinhard M, Schumacher FK, Rutsch S, et al (2014) Spatial mapping of dynamic cerebral
604 autoregulation by multichannel near-infrared spectroscopy in high-grade carotid artery disease. *J*
605 *Biomed Opt* 19:097005. doi: 10.1117/1.JBO.19.9.097005
- 606 Roebroek A, Formisano E, Goebel R (2005) Mapping directed influence over the brain using Granger
607 causality and fMRI. *Neuroimage* 25:230–42. doi: 10.1016/j.neuroimage.2004.11.017
- 608 Rossini PM, Altamura C, Ferretti A, et al (2004) Does cerebrovascular disease affect the coupling
609 between neuronal activity and local haemodynamics? *Brain* 127:99–110. doi:
610 10.1093/brain/awh012
- 611 Santosa H, Aarabi A, Perlman SB, Huppert TJ (2017) Characterization and correction of the false-
612 discovery rates in resting state connectivity using functional near-infrared spectroscopy. *J*
613 *Biomed Opt* 22:55002. doi: 10.1117/1.JBO.22.5.055002

- 614 Sato T, Nambu I, Takeda K, et al (2016) Reduction of global interference of scalp-hemodynamics in
615 functional near-infrared spectroscopy using short distance probes. *Neuroimage* 141:120–132.
616 doi: 10.1016/j.neuroimage.2016.06.054
- 617 Satterthwaite TD, Wolf DH, Loughead J, et al (2012) Impact of in-scanner head motion on multiple
618 measures of functional connectivity: relevance for studies of neurodevelopment in youth.
619 *Neuroimage* 60:623–32. doi: 10.1016/j.neuroimage.2011.12.063
- 620 Schelter B, Winterhalder M, Eichler M, et al (2006) Testing for directed influences among neural
621 signals using partial directed coherence. *J Neurosci Methods* 152:210–9. doi:
622 10.1016/j.jneumeth.2005.09.001
- 623 Schippers MB, Renken R, Keysers C (2011) The effect of intra- and inter-subject variability of
624 hemodynamic responses on group level Granger causality analyses. *Neuroimage* 57:22–36. doi:
625 10.1016/j.neuroimage.2011.02.008
- 626 Scholkmann F, Kleiser S, Metz AJ, et al (2014) A review on continuous wave functional near-infrared
627 spectroscopy and imaging instrumentation and methodology. *Neuroimage* 85 Pt 1:6–27. doi:
628 10.1016/j.neuroimage.2013.05.004
- 629 Schumacher FK, Schumacher LV, Schelter BO, Kaller CP (2019) Functionally dissociating ventro-
630 dorsal components within the rostro-caudal hierarchical organization of the human prefrontal
631 cortex. *Neuroimage* 185:398–407. doi: 10.1016/j.neuroimage.2018.10.048
- 632 Scouten A, Papademetris X, Constable RT (2006) Spatial resolution, signal-to-noise ratio, and
633 smoothing in multi-subject functional MRI studies. *Neuroimage* 30:787–793. doi:
634 10.1016/j.neuroimage.2005.10.022
- 635 Smith SM, Bandettini PA, Miller KL, et al (2012) The danger of systematic bias in group-level fMRI-
636 lag-based causality estimation. *Neuroimage* 59:1228–1229. doi:
637 10.1016/j.neuroimage.2011.08.015
- 638 Stokes PA, Purdon PL (2017) A study of problems encountered in Granger causality analysis from a

- 639 neuroscience perspective. *Proc Natl Acad Sci* 114:E7063–E7072. doi: 10.1073/pnas.1704663114
- 640 Sutoko S, Chan YL, Obata A, et al (2019) Denoising of neuronal signal from mixed systemic low-
641 frequency oscillation using peripheral measurement as noise regressor in near-infrared imaging.
642 *Neurophotonics* 6:015001. doi: 10.1117/1.NPh.6.1.015001
- 643 Takahashi T, Takikawa Y, Kawagoe R, et al (2011) Influence of skin blood flow on near-infrared
644 spectroscopy signals measured on the forehead during a verbal fluency task. *Neuroimage*
645 57:991–1002. doi: 10.1016/j.neuroimage.2011.05.012
- 646 Tong Y, Frederick BD (2010) Time lag dependent multimodal processing of concurrent fMRI and
647 near-infrared spectroscopy (NIRS) data suggests a global circulatory origin for low-frequency
648 oscillation signals in human brain. *Neuroimage* 53:553–64. doi:
649 10.1016/j.neuroimage.2010.06.049
- 650 Tong Y, Hocke LM, Licata SC, Frederick B deB (2012) Low-frequency oscillations measured in the
651 periphery with near-infrared spectroscopy are strongly correlated with blood oxygen level-
652 dependent functional magnetic resonance imaging signals. *J Biomed Opt* 17:106004. doi:
653 10.1117/1.JBO.17.10.106004
- 654 Tong Y, Hocke LM, Nickerson LD, et al (2013) Evaluating the effects of systemic low frequency
655 oscillations measured in the periphery on the independent component analysis results of resting
656 state networks. *Neuroimage* 76:202–215. doi: 10.1016/j.neuroimage.2013.03.019
- 657 Webb JT, Ferguson M a, Nielsen J a, Anderson JS (2013) BOLD Granger causality reflects vascular
658 anatomy. *PLoS One* 8:e84279. doi: 10.1371/journal.pone.0084279
- 659 Winder AT, Echagarruga C, Zhang Q, Drew PJ (2017) Weak correlations between hemodynamic
660 signals and ongoing neural activity during the resting state. *Nat Neurosci* 20:1761–1769. doi:
661 10.1038/s41593-017-0007-y
- 662 Zhang Q, Strangman GE, Ganis G (2009) Adaptive filtering to reduce global interference in non-
663 invasive NIRS measures of brain activation: How well and when does it work? *Neuroimage*

664 45:788–794. doi: 10.1016/j.neuroimage.2008.12.048

665